Cell Reports
Physical Science

CellPress
OPEN ACCESS

Article

Three-dimensional SEI framework induced by ion regulation in toroidal magnetic field for lithium metal battery

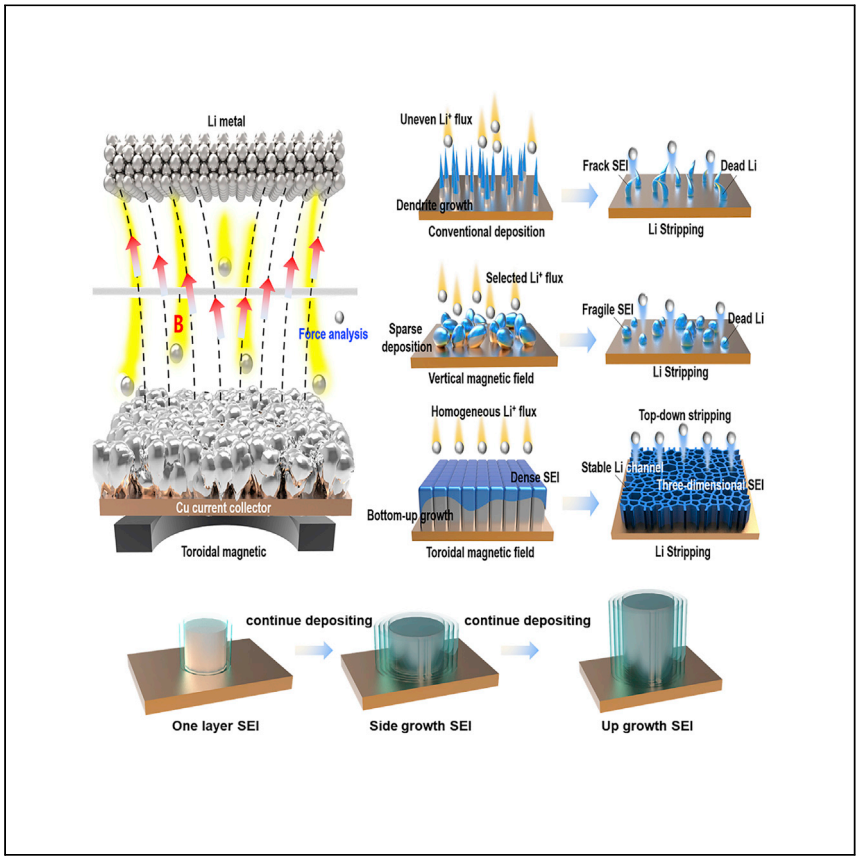

Ultra-dense lithium deposition and high concentration of anions on the surface of the collector can promote the formation of three-dimensional SEI framework. Li et al report the effects of toroidal magnetic fields on SEI framework structure and subsequent electrode performance.

Yan Li, Manjie Xiao, Chunli Shen, ..., Liqiang Mai, Yan Zhao, Xu Xu

mlq518@whut.edu.cn (L.M.)
yan2000@whut.edu.cn (Y.Z.)
xuxu@whut.edu.cn (X.X.)

Highlights

Three-dimensional SEI framework can be achieved under toroidal magnetic field

Three-dimensional SEI maintains cyclic stability after removal of the magnet

This 3D SEI can realize 1,300 cycles at a high current density of 50 mA/cm^2

Li et al., Cell Reports Physical Science 3, 101080
October 19, 2022
https://doi.org/10.1016/j.xcrp.2022.101080

Cell Reports
Physical Science

CellPress
OPEN ACCESS

Article

Three-dimensional SEI framework induced by ion regulation in toroidal magnetic field for lithium metal battery

Yan Li,[1,4] Manjie Xiao,[1,4] Chunli Shen,[1] Lianmeng Cui,[1] Wei Yang,[1] Chi Zhang,[2] Xinhui Chen,[1] Liqiang Mai,[1,*] Yan Zhao,[1,2,*] and Xu Xu[1,3,*]

SUMMARY

Lithium metal batteries are considered to have great potential as rechargeable batteries in next-generation energy storage devices. However, the generation of dead lithium and lithium dendrites caused by the rupture of the solid-electrolyte interphase (SEI) during cycling limits the application of lithium metal batteries. While tremendous efforts have been devoted to modification of SEI, the long-term and stable use of residual SEI has rarely been studied. Herein, we design a LiF-rich three-dimensional SEI framework (3DSF) formed in a toroidal magnetic field. This 3DSF can induce the uniform bottom-up deposition of lithium metal in the channel structure and realize 1,300 cycles at a high current density of 50 mA/cm^2. The capacity of the battery paired with a high mass-loading $LiFePO_4$ cathode (18.3 mg/cm^2) maintains 98.2% at 1 C after 150 cycles. This work provides a simple and practical strategy for the additive free development of lithium metal battery technology.

INTRODUCTION

Lithium ion batteries have the disadvantage of low energy density owing to the principle of intercalation chemistry, which limits the further development of portable electronic devices and electric vehicles.[1–4] Therefore, to meet the requirements of higher energy density, it is generally believed that lithium metal batteries have sufficient potential to become a new generation of energy storage systems.[5–7] Lithium metal anode has a high theoretical capacity and a low redox potential, known as the "holy grail" in battery materials.[8–10] However, two serious problems in the cycling process of lithium metal batteries have been hindering their further commercial applications.[11–13] The first one is that the organic components in the solid-electrolyte interphase (SEI) layer produced by the contact between the electrolyte and the lithium metal are prone to crack, leading to the re-contact of the lithium with the electrolyte and the unrestricted generation of SEI. This will lead to the continuous loss of lithium source and rapid capacity decay of the lithium metal battery. Second, the rapid growth of lithium dendrites will puncture the separator and cause short circuit, resulting in serious safety problems. To address these two problems, many efforts have focused on three-dimensional current collectors,[14–21] electrolyte additives in order [22–26] and artificial SEI layers[27–30] in recent years. Three-dimensional current collectors with high specific surface area and abundant active sites enable uniform deposition of Li near the electrode surface. The electrolyte additives can form a more stable SEI. The strategy of artificial SEI is to block the direct contact between the electrolyte and lithium metal to inhibit the growth of lithium metal dendrites. However, each of these three solutions introduce extra battery components,

[1]State Key Laboratory of Advanced Technology for Materials Synthesis and Processing, International School of Materials Science and Engineering, Wuhan University of Technology, Hubei 430070, China

[2]The Institute of Technological Sciences, Wuhan University, Hubei, Wuhan 430072, China

[3]Lead Contact

[4]These authors contribute equally to this work.

*Correspondence: mlq518@whut.edu.cn (L.M.), yan2000@whut.edu.cn (Y.Z.), xuxu@whut.edu.cn (X.X.)

https://doi.org/10.1016/j.xcrp.2022.101080

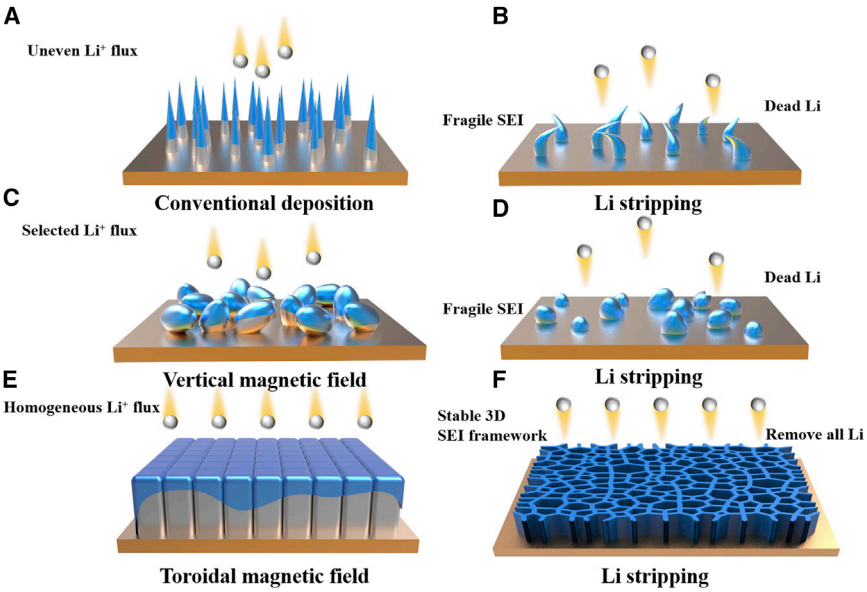

Figure 1. Schematic diagram of lithium depositing/stripping behaviors under different magnetic field situations

(A–F) (A) Li deposition behaviors without magnetic field, (B) Li stripping behaviors without magnetic field, (C) Li deposition behaviors with VMF, (D) Li stripping behaviors with VMF, (E) Li deposition behaviors with TMF, (F) Li stripping behaviors with TMF.

which increase the battery cost and weight, and are not conducive to the commercialization of lithium metal batteries. Most researchers believe that the naturally formed SEI is not conducive to the cycling performance of lithium metal batteries. However, LiF,[31–33] Li_2O,[34] and other inorganic components in natural SEI have been proved to have good mechanical strength and lithium ion conductivity. If these characteristics of residual SEI can be used to guide the transport and deposition of lithium ions, it will allow us to "turn waste into treasure" without additional costs.

Herein, a toroidal magnetic field (TMF) is introduced to regulate the motion behaviors of the ions, which results in the planarized ultra-dense growth of lithium metal and generates LiF-rich three-dimensional SEI framework (3DSF). The pore size and thickness of the 3DSF can be precisely controlled by the current density and deposition capacity. The 3DSF has high ionic conductivity, which can induce the growth of lithium metal inside the pores without dendrites from bottom to top in the subsequent cycles. The 3DSF has strong mechanical strength and maintains its morphology during multiple lithium deposition and desorption processes. With 3DSF constructed by the TMF, the lithium metal battery exhibits superior electrochemical performance, and the lithium symmetric battery can withstand an ultra-high current density of 50 mA/cm^2 for more than 1,300 cycles. It can cycle 1,000 times at a current density of 3 C when paired with the lithium iron phosphate cathode. Combined with the above-mentioned cost-free improvement and performance enhancement, we believe this research can promote the commercialization of lithium metal battery.

RESULTS AND DISCUSSION

Formation mechanism of 3DSF under TMF

As illustrated in Figure 1, the deposition and stripping behaviors of lithium metal under three different magnetic field conditions (no magnetic field, vertical magnetic field [VMF], and TMF) are compared. With no magnetic field, the lithium ions are

completely affected by the local high current, and an uneven flux of Li^+ will appear on the surface of the current collector, resulting in the growth of lithium dendrites. At the stripping stage, the dendrite-like SEI shell are prone to being crushed, and the remaining lithium metal become dead lithium owing to the disconnection from the current collector (Figures 1A and 1B). Under the VMF, the growth of lithium dendrites is inhibited. However, lithium metal exhibits sparse deposition and irregular spheres form around the current collector protrusions because of the selected Li^+ flux. After the lithium is stripped, a fragile and irregular SEI layer is left, along with the dead lithium (Figures 1C and 1D). Under the TMF, the lithium metal exhibits a planar and bottom-up growth on account of the homogeneous Li^+ flux. After Li stripping, a stable and dense 3DSF structure is formed. During stripping, lithium is uniformly peeled off layer by layer from top to bottom and the 3DSF structure is kept. Even if the TMF is removed during the subsequent Li redepositing process, Li ions can be uniformly deposited under the induction of stable Li channels provided by the 3DSF (Figures 1E and 1F). Based on the particularity of TMF, two factors are believed to contribute to the formation of 3DSF: "the disorder homogenization effect of lithium ions" and the "slow ion diffusion effect."

In recent years, many works have focused on the application of VMFs in lithium metal anodes.[35–40] Owing to the existence of lithium dendrites, lithium ions are attracted by the local high current, which promotes the growth of lithium dendrites (Figure S1A). The VMF can make the lithium ions deviating from the magnetic field line and move in a circular motion around the tip owing to the Lorentz force. The velocity of the horizontal direction can slightly resist the attraction of the lithium dendrite (Figure S1B). However, just like a meteorite that strays into the gravitational range of a black hole, Li ions are often difficult to get rid of the attraction of lithium dendrites, which further promotes the growth of lithium dendrites. In the final analysis, it is because the velocity of getting rid of the attraction of lithium dendrites under the VMF is not fast enough. According to the Lorentz force formula:

$$F = QV_aB, \quad \text{(Equation 1)}$$

where Q is the charged amount of the Li ion, B is the magnetic field strength, and V_a is the velocity of the Li ion in the direction perpendicular to the magnetic field when the ion is moving. Combined with the formula for the circular motion of the particle:

$$F = mV_b^2/r, \quad \text{(Equation 2)}$$

where m is the mass of the Li ion, V_b is the velocity of the Li ion in circular motion, which can be understood as the velocity of getting rid of the lithium dendrite attraction, and r is the radius of the Li ion's circular motion. Substituting Equation (2) into Equation (1), we have:

$$QV_aB = mV_b^2/r. \quad \text{(Equation 3)}$$

In general, V_b, the velocity to get rid of the dendrite attraction, is positively related to the V_a, which is perpendicular to the direction of the magnetic field line. In the VMF, V_a is generated by the attraction of the tip, which is a process with a short time and a short acceleration path. However, in the TMF, since the direction of the magnetic field is not parallel to the movement direction of the lithium ions at the initial position, the lithium ions fall in a spiral motion after entering the magnetic field, and the V_a will increase with the driving of the electric field force. The V_b is much larger than the escape velocity in the VMF, so Li ion can get rid of the attraction of the local high current at the lithium dendrites. Therefore, lithium ions can be uniformly deposited in the form of spiral motion under the TMF (Figure S1C), which is defined as the disorder homogenization effect of lithium ions.

In contrast, the anion ($TFSI^-$) in the solution will also be affected by the magnetic field, so the $TFSI^-$ ions in the electrolyte also have a spiral motion under the TMF. However, unlike lithium ions, $TFSI^-$ ions suffer a much greater resistance from the electrolyte owing to their larger volume. More important, the spiral motion orbit of $TFSI^-$ will increase the movement path of the ion, decreasing the transference number of $TFSI^-$ because of the additional drag effect of the electrolyte (Figure S2A). Compared with the scenarios without magnetic field and in the VMF, the transference ratios of Li ions to $TFSI^-$ are basically unaffected (Figure S2B). To verify that the Li^+ and $TFSI^-$ will increase the movement path, COMSOL simulation was completed to show the trajectories of ions (Figure S3). In the absence of a magnetic field, the ions fall toward the center, which has the local high current density area. And this also indicates the reason for the rapid growth of lithium dendrites in the absence of a magnetic field (Figure S3B). The VMF enhances the resistance to the attraction of the localized high current area, but the movement path of the ions becomes smaller (Figure S3C). This results in Li metal exhibiting sparse deposition and irregular sphere formation. However, the ions are in a downward spiral state under the TMF, which greatly increases the travel path (Figure S3A). The transference of $TFSI^-$ is greatly hindered under the resistance of the electrolyte. Since the total current density through the electrolyte solution is the sum of the current densities of positive and anion transference. Therefore, the decrease in the $TFSI^-$ transference number means an increase in the transference number of lithium ions. As shown in Figures S4A and S4B, the lithium ion transference number of the lithium Li||Li symmetric battery was tested. Under the TMF, the lithium ion transference number is as high as 0.90, while the lithium ion transference number in the absence of magnetic field is 0.66. It can be seen that the addition of the TMF can indeed effectively increase the lithium ion transference. So, the effect of the TMF on reducing the $TFSI^-$ ion transference number is called the slow ion diffusion effect. Many works have reported that enhancing the lithium ion transference number can effectively suppress the growth of lithium dendrites. If the lithium ions migrate fast enough in the electrolyte, the lithium ion concentration gradient around the electrode is small. This results in the unoriented and bulk growth of the lithium metal. The TMF practically accelerates the transference of lithium ions, which can provide sufficient lithium ions with a low concentration gradient even during high current density deposition, suppressing the lithium dendrite formation. The TMF can also reduce the exchange current density at the electrode surface. As shown in Figures S4C and S4D, the exchange current density of the Li||Li symmetric battery is 0.33 mA/cm^2 under the TMF, which is nearly three times less than the exchange current density (1.04 mA/cm^2) without the magnetic field. Owing to the slow ion diffusion effect, it can accelerate the transport of lithium ions on the electrode surface, decrease the lithium ion concentration polarization (C_b Li^+/C_s Li^+), and then decrease the exchange current density. At low exchange current density, the lithium deposition exhibits a low aspect ratio structure. Compared with Li dendrites, this uniform bulk structure can in turn lead to more uniform local current density distribution, decreasing the surface electric field distortion and enabling more uniform Li metal growth. To macroscopically observe the growth of lithium under TMF, *in situ* optical microscopic images of Li||Cu battery at 20 mA/cm^2 are exhibited in Figure S5. The lithium dendrite formed on the copper foil after 5 min and grew rapidly into a forest shape within 30 min (Figure S5A). In contrast, the copper foil showed flat growth with no visible dendrites for 30 min at such a large current density under TMF (Figure S5B). More important, under the same deposition capacity, the thickness of the lithium layer with TMF is much lower than that of the battery without the influence of the magnetic field.

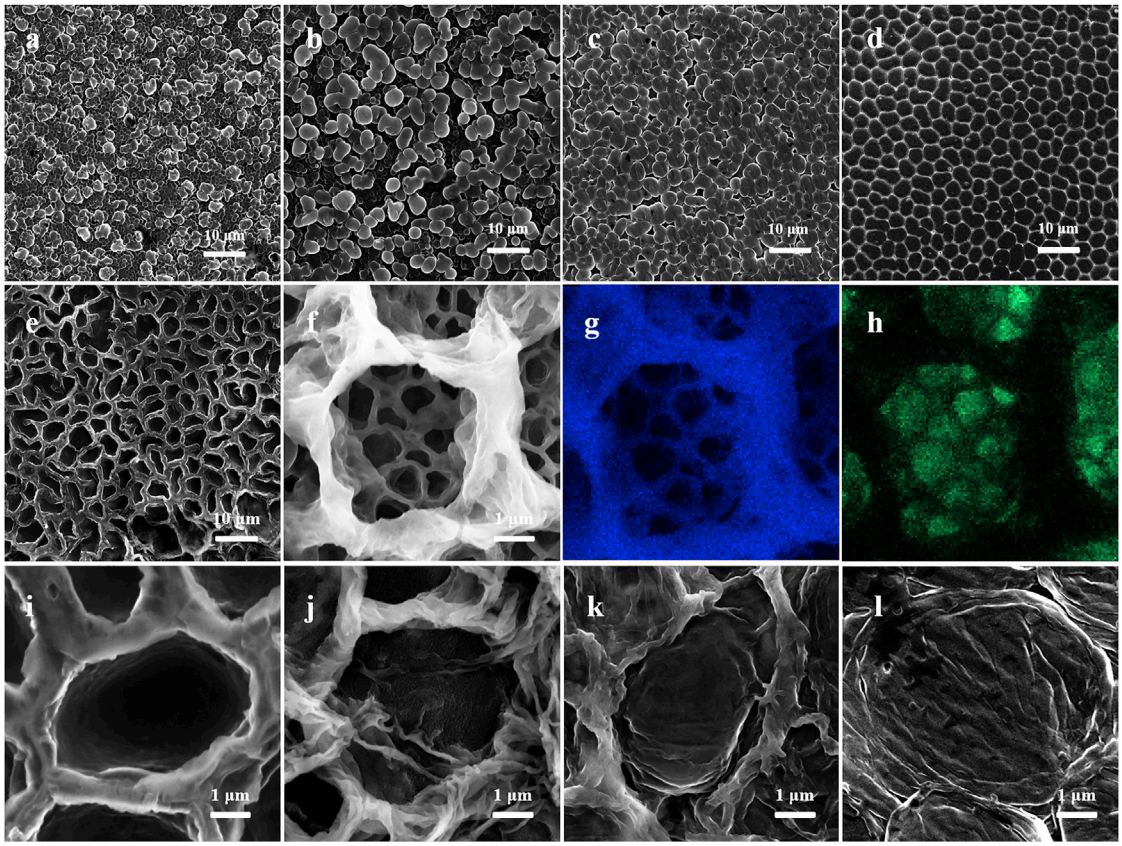

Figure 2. SEM images of the lithium deposition with TMF

(A–D) (A) 15 min, (B) 30 min, (C) 45 min, and (D) 60 min at 1 mA/cm^2.

(E–H) (E) SEM images of 3DSF after stripping Li, (F) magnified SEM images of the 3DSF, (G) F element mapping, and (H) Cu element mapping.

(I–L) SEM images of the lithium deposition in 3DSF without TMF for (I) 15 min, (J) 30 min, (K) 45 min, and (L) 60 min.

Characterization of lithium deposition and 3D SEI framework

To explore the growth process of lithium metal under the TMF, Figures 2A–2D present the scanning electron microscopy (SEM) images of electrodepositing for 15 min, 30 min, 45 min, and 60 min at a current density of 5 mA/cm^2, respectively. It can be observed that, when deposited for 15 min, lithium metal has been deposited as two layers. The lower layer is an ultra-dense structure, as mentioned. The upper layer exhibits a cylindrical structure with a larger volume than that of the lower layer. As the lithium deposition continues, the diameter and number of lithium block increase, the lithium deposition becomes denser, and finally the ultra-dense packing is formed again. The white boundary between the lithium block is the new 3DSF formed further. When all the lithium is completely stripped, it can be seen that the 3DSF can be completely preserved (Figure 2E). The planarized growth of lithium metal can induce the formation of 3DSF. As shown in Figure S6, the lithium metal nucleates and grows into a small cylinder, and a thin layer of SEI is formed on the top and sides. When lithium ions continue to be deposited, the column shows a side growth, and the side SEI is prone to be broken owing to the poor mechanical strength. A new layer of SEI is generated owing to the re-contact of the electrolyte with the lithium metal. This SEI growth mode not only increases the thickness of the SEI layer, but also increases the mechanical strength of the SEI layer. When the mechanical strength of the SEI is sufficient to resist the planar growth of lithium metal or being squeezed by other lithium cylindrical SEIs, the lithium metal continues to grow

upward. The growth height is proportional to the deposition capacity of the lithium metal and the SEI will also grow upward. As a result, a new 3DSF structure with high mechanical strength and excellent chemical stability that can induce the in situ growth of lithium metal was successfully constructed. In Figure 2F, there are many small holes inside the large holes, which indicates that the formed 3DSF is a hierarchical porous structure. The holes gradually become larger from the bottom to the top. This is because the lower layer's lithium blocks have smaller bulk diameters, and the upper layer continues to be ultra-dense deposition in the form of larger diameter lithium block. The element-mapping test on this structure was performed, and the distributions of C, N, O, and F elements are completely consistent with the SEI and the smaller holes at the bottom are consistent with the distribution of exposed copper (Figures 2G, 2H, and S7). This indicates that the lithium in the pores is completely stripped and there is basically no dead lithium. To observe the deposition of lithium in 3DSF, the completely stripped current collector without TMF at same current density was deposited from 15 to 60 min. As shown in the SEM images (Figures 2I–2l), with the increase of deposition capacity, Li metal could be deposited uniformly and dendrite-free from bottom to top in the SEI framework. This shows that 3DSF can well induce the uniform deposition of Li metal without magnetic field.

To further explore the effect of current density and deposition capacity on the morphology of lithium deposition, the current collector was deposited at 1 mA/cm^2 for 1, 5, 10, 20, and 50 h, respectively, and the SEM images of their top surface and cross-section topography were shown in Figure S8. It can be seen that the diameter and thickness of the lithium block increases proportionally with the deposition capacity. To more intuitively compare the effect of deposition capacity on the deposition morphology of the lithium block, the relation between the diameter and thickness of the lithium block is shown in Figure 3A. It can be seen that when the deposition capacity reaches 1 mAh/cm^2, 5 mAh/cm^2, 10 mAh/cm^2, 20 mAh/cm^2, and 50 mAh/cm^2, the diameter of the lithium block increases to 4.6, 7.5, 10.3, 14.1, and 20.3 μm, respectively. The thickness also increases to 5.4, 31.9, 65.7, 110.6, and 217.1 μm, respectively. It can be concluded that when the deposition capacity increases, Li metal always exhibits ultra-dense depositing under the 3DSF. Subsequently, lithium metal with a capacity of 5 mAh/cm^2 was deposited at different current densities of 2 mA/cm^2, 5 mA/cm^2, 10 mA/cm^2, 20 mA/cm^2, and 50 mA/cm^2, respectively. Their top surface and cross-section topography were observed by SEM in Figures S8K–S8T. It can be seen that the diameter of the lithium block decreases with the increase of the current density, which is 6.9, 4.9, 3.9, 2.4, and 1.7 μm, respectively. While the thickness is kept at around 30 μm owing to the control of the deposition capacity at 5 mAh/cm^2 (Figure 3B). With the high deposition current density, the lithium metal also exhibits a uniform deposition under TMF. When increasing the current density, it means that more lithium is deposited on the current collector at the same time, resulting in an increase in the nucleation sites on the current collector and then the ultra-dense deposition of lithium metal is completed in a short time. This is why the diameter of the lithium block decreases with the increasing of current density. While the thickness of the lithium block is positively correlated with the lithium deposited capacity. When deposited at the same current density, the diameter of the lowest lithium layer formed on the current collector is the same. As the deposition capacity increases, the number of lithium layers also increases and the diameter of the lithium block in each layer increases accordingly. When the deposition amount is large enough, the diameter of the lithium block gradually increases from the current collector to the top. After all the lithium is stripped, the pore size of the formed 3DSF also increases gradually. This means

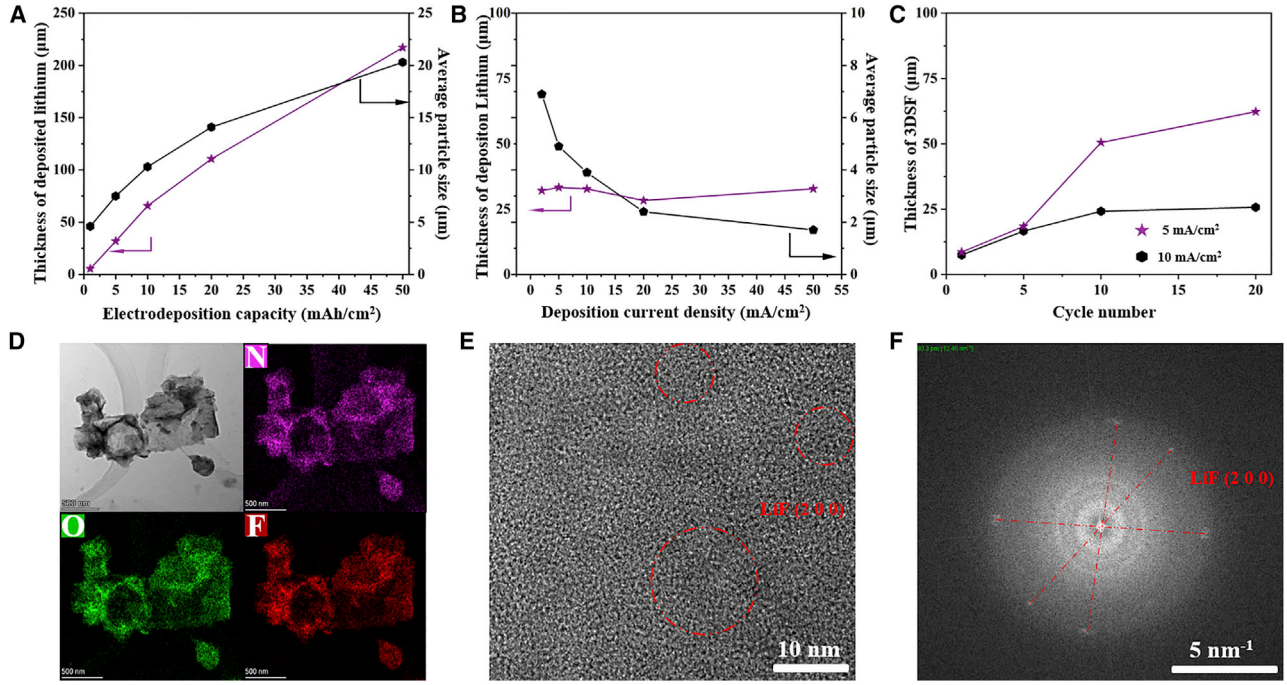

Figure 3. The line graphs about thickness and 3DSF characterization by TEM

(A) Lithium thickness and particle diameter in 1 mA/cm^2 for 1, 5 10, 20, and 50 h.

(B) Lithium thickness and particle diameter in 2, 5, 10, 20, and 50 mA/cm^2 for the deposition capacity of 5 mAh/cm^2.

(C) The 3DSF thickness with the electrodeposition capacity for 1, 5, 10, and 20 h.

(D) The TEM and element mapping images of 3DSF.

(E) The HRTEM images of 3DSF.

(F) The selected-area electron diffraction patterns of 3DSF.

the thickness and pore size of the 3DSF can be tunable by controlling the current density and deposition capacity.

To verify that the 3DSF did not grow infinitely with Li depositing and stripping, lithium metal was stripped after 1 h of deposition at 5 mA/cm^2 and 10 mA/cm^2, respectively. The deposition and stripping times were subsequently increased to 1, 5, 10, and 20 h and the cross-section images of the 3DSF were observed by SEM (Figure S9). The relation between the electrodeposition capacity and thickness of the 3DSF is shown in Figure 3C. After the first deposition and stripping at 5 mA/cm^2 and 10 mA/cm^2, the thickness of the 3DSF reached 7.4 and 8.6 μm, respectively, and then reached 16.6 and 18.3 μm after the fifth deposition and stripping cycles. The difference in thickness is not obvious. But when it came to the tenth times, the thickness was only 24.2 μm at 5 mA/cm^2, while the thickness of 10 mA/cm^2 reaches 50.5 μm. The thickness of the lithium block with the deposition amount of 5 mAh/cm^2 and 10 mAh/cm^2 was 31.5 and 65.9 μm, respectively. It showed that the current density during deposition is not related to the growth rate of 3DSF, but the deposition capacity (thickness of the lithium block) limits the growth of the thickness of the 3DSF. The thicknesses of the structures reached 25.7 μm and 62.3 μm after the twentieth deposition and stripping, respectively. This shows that the growth rate of 3DSF is limited by the thickness of the lithium block with the same deposition capacity, which means that the growth of the 3DSF can be controlled. The transmission electron microscopy (TEM) was also carried to explore the composition of the 3DSF. As shown in Figure 3D, its main components are N, O, and F elements, which are uniformly distributed on 3DSF, and it is consistent with the

traditional SEI element composition. Figure 3E is a high-resolution TEM (HRTEM) characterization, and the SEI structure contains a large amount of LiF. Typically, the lattice spacing of 0.202 nm can be ascribed to a (2 0 0) lattice plane. The presence of LiF in this pattern is also verified by selected area electron diffraction (Figure 3F).

To gain an in-depth understanding of the composition of the 3DSF, *in situ* X-ray photoelectron spectroscopy (XPS) etching technology was used to characterize the 3DSF and the common SEI structure. The results were shown in Figures 4A and S10. Before the common SEI structure etching, the signals of $ROCO_2Li$, C-C/C-H, C-O, and C=O were detected in the C element (Figure S10), and the content of $ROCO_2Li$ is the highest, which means that the common SEI surface contains a large amount of organic component. With the increase of etching time, the composition of $ROCO_2Li$ gradually decreases. In the F element spectrum, the surface contains a large amount of $–CF_3$. When the etching time reaches 50 s, a high content of LiF appears and then gradually decreases with the increase of the etching depth. From the N element spectrum, the content of Li_3N and LiN_xO_y gradually decreases with the etching depth from 0 s to 200 s. In the O spectrum, the surface before etching contains a lot of Li_2CO_3 and O-C=O structure. With the increase of etching depth, the composition of Li_2O gradually increases and the composition of organic components slowly decays. Based on the etching results of the four elements (C, N, O, and F) in common SEI layer, it can be inferred that the element distribution of the common SEI layer is roughly divided into the double-layer structure. The outer layer is an organic layer that is easily broken, and the inner layer is an inorganic layer of Li_2O, LiF with stable mechanical strength. Among them, Li_3N and organic component are embedded in the entire SEI composition. Figure 4B is the histogram of the element content with the etching time. It can be seen that the C element content on the surface reached 41.2%. It means the surface contains a large amount of $–CF_3$ and organic components. After etching, the content of O element increases, while the content of C element decreases slightly, indicating that the underlying inorganic layer SEI is composed of a large amount of Li_2O. This structure is prone to the generation of dead lithium from the rupture of the SEI. Similarly, in situ XPS etching tests on the 3DSF was carried out. The content of $ROCO_2Li$ in the unetched 3DSF in the C spectrum is low and the C content decreases rapidly with the etching (Figure 4A). In the F spectrum, the surface contains a large amount of $–CF_3$ and then high LiF peaks appears after etching, which is similar to the XPS result of the common SEI. In the N spectrum, a large amount of Li_3N, a small amount of LiN_xO_y and $LiNO_2$ can be observed on the surface, indicating that $LiNO_3$ had been reduced. As the etching depth increases, the composition of each component gradually decreases. The O spectrum shows that there are some organic component and Li_2CO_3 on the surface before etching. But with the deepening of etching, the two components are gradually converted into Li_2O. As shown in Figure 4C, before the etching, the C and O elements accounted for 21.9% and 31.9%, respectively. The reason is that the surface of the 3DSF has a part of the organic layer. As the etching depth increases, the LiF content increases greatly, and a small part of Li_2O existed. Compared with the common SEI, the content of organic layer components of 3DSF is extremely low. And the content of F element is as high as 88.3%, which means that the interior of 3DSF is basically composed of LiF. LiF is an inorganic lithium salt, which is denser than organic components. And it has higher mechanical strength, which is more difficult to decompose in complex electrochemical reactions. So it is easier to form a stable SEI structure.[41] The organic layer exists only at the top of the 3DSF. The 3DSF composed of LiF has good mechanical strength and ionic conductivity, which can also induce the uniform dendrite-free deposition of lithium metal.

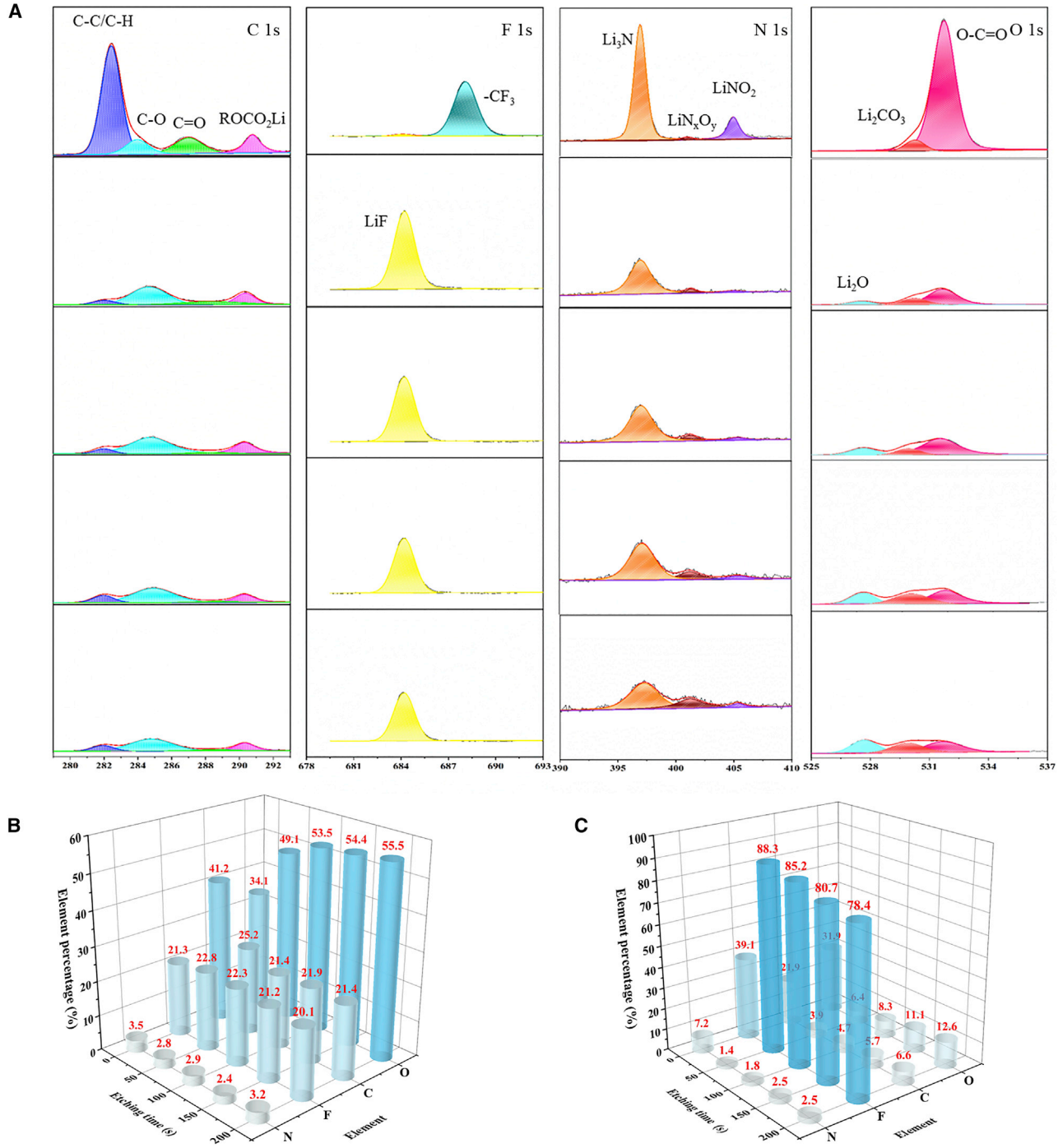

Figure 4. In-situ XPS etching tests for C, F, N, and O elements and element content distribution

(A–C) (A) In-situ XPS etching at 0, 50, 100, 150, and 200 s on 3DSF. The histogram of the element ratio for N, F, C, and O elements at 0, 50, 100, 150, and 200 s on (B) common SEI structure (C) 3DSF.

Electrochemical performance of lithium metal battery with 3DSF

To verify that the LiF-rich 3DSF can improve the electrochemical performance of lithium metal battery, various electrochemical tests were designed. First, to explore the influence of the TMF on the electrochemical performance of the battery after the 3DSF is stably formed, the cycling performances of the lithium metal batteries were compared at

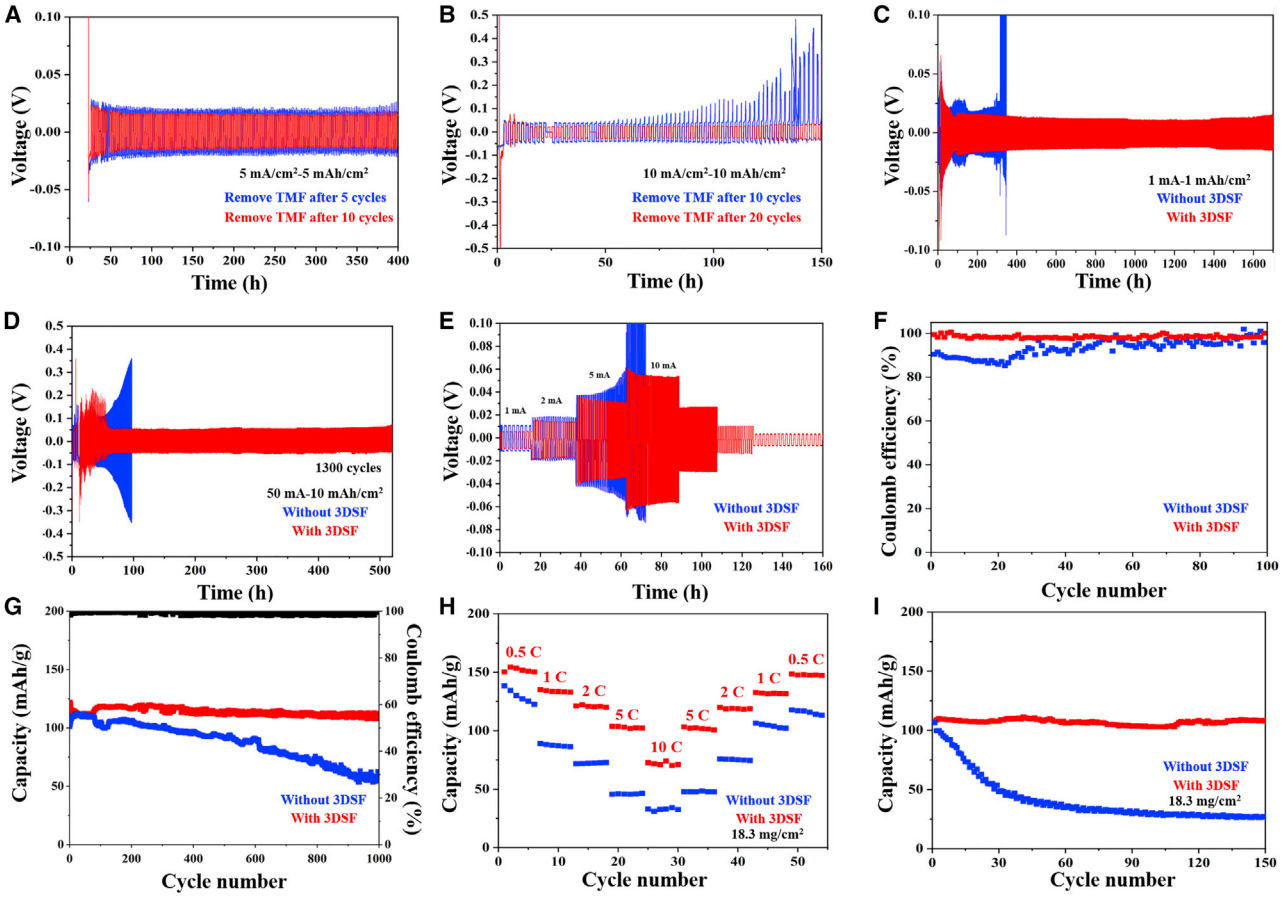

Figure 5. Cycling performances of the Li||Li symmetric battery

(A and B) (A) 5 mA/cm^2-5 mAh/cm^2, (B) 10 mA/cm^2-10 mAh/cm^2 for removing TMF after a certain cycles.

(C and D) (C) Cycling performances of the Li||Li symmetric battery at (c) 1 mA/cm^2–1 mAh/cm^2, (D) 50 mA/cm^2–10 mAh/cm^2.

(E–G) (E) Rate performances of Li||Li symmetrical battery from 1 mA/cm^2-1 mAh/cm^2 to 10 mA/cm^2–1 mAh/cm^2 (F) CE of Li||Cu battery at 1 mA/cm^2–1 mAh/cm^2, (G) long cycle performances of LFP full battery at 3 C.

(H) Rate performances of LFP full battery (18.3 mg/cm^2) from 0.5 C to 10 C.

(I) Long cycle performances of LFP full battery (18.3 mg/cm^2) at 1 C.

1 mA/cm^2–1 mAh/cm^2 with and without the removal of the TMF after 10 cycles (Figure S11). And the magnet shape, placement position and magnetic flux of the magnet are shown in the Figure S12. Taking the battery, which cycled with the same current density under TMF as the control sample, it is found that there is no obvious difference in the electrochemical performance between them. This indicates that TMF was only used to form the stable 3DSF to induce the uniform deposition of lithium metal. From the perspective of commercialization, the TMF is used to construct a stable and appropriate 3DSF in the subsequent tests and can be removed during the following service life. Second, to prove that the performance of the lithium metal battery can also remain stable without TMF after the complete 3DSF was formed, the lithium metal battery cycled for 5 and 10 times at 5 mA/cm^2–5 mAh/cm^2 (the number of cycles correspond with the different thicknesses of the 3DSF) and then the TMF was removed (Figure 5A). The other experiment is that the lithium metal battery was cycled at 10 mA/cm^2–10 mAh/cm^2 for 10 and 20 cycles before removing the TMF to study the cycle performances of the lithium metal batteries (Figure 5B). The difference from Figure 5A is that the lithium metal battery with TMF removed after 10 cycles shows a severe polarization. However, the lithium metal battery with TMF removed after 20 cycles still maintains a good cycle performance.

Combined with the previous conclusions, the thickness of the 3DSF formed by 10 cycles at 10 mAh/cm^2 is 50.5 μm (Figure S9G), while the thickness of lithium metal with 10 mAh/cm^2 deposition capacity is 65.7 μm (Figure S8H). When the thickness of Li metal is higher than that of the 3DSF, the 3DSF has limited effect on the deposition of excess Li metal. However, after 20 cycles of deposition and stripping, the thickness of the 3DSF reaches 62.3 μm, which is similar to the thickness of lithium metal with a deposition capacity of 10 mAh/cm^2. Therefore, the 3DSF is complete enough to guide the uniform deposition of lithium metal. When the 3DSF is formed completely enough with the TMF and the thickness of lithium metal is lower than that of the 3DSF in the deposition and stripping process, the lithium metal battery can still maintain a stable cycle in the absence of TMF and this almost cost-free design is more conducive to commercial applications. To verify that this 3DSF can enhance the cycling stability of Li metal battery, the electrochemical performance tests of Li||Li symmetric battery and Li||Cu battery during Li depositing and stripping were also designed. As shown in Figure 5C, the Li||Li symmetric battery has a stable deposition and stripping performance at a low current density and capacity of 1 mA/cm^2–1 mAh/cm^2 for 1,700 h with the 3DSF, while the battery has severe polarization at around 350 h without 3DSF, leading to the battery failure. At a high current density, lithium ions will cause dendrite growth owing to the high concentration gradient. Therefore, the stability of the electrode at high current density is an important part of measuring the performance of lithium metal battery. In Figure 5D, the current density was increased to 50 mA/cm^2 with an area capacity of 10 mAh/cm^2. It can be seen that the battery without 3DSF failed at 100 h because of the large polarization voltage, but the battery with 3DSF kept the voltage stable during the 1,300 times cycling in 520 h. The rate performance was shown in Figure 5E. The voltage polarization of the battery with 3DSF remained stable from 1 mA/cm^2 to 10 mA/cm^2, while the battery without 3DSF had severe polarization when the current density reached 10 mA/cm^2. The above series of electrochemical performance verifies that the 3DSF formed under the TMF can maintain the cycle stability in the process of high current density or low-to-high current density conversion, and the 3DSF can be effective and stable for a long time to accelerate the mass transfer of lithium ions, so that lithium metal grows in the framework and fundamentally inhibits the formation of lithium dendrites. To further verify the commercialization potential of the 3DSF in lithium metal battery, the Coulombic efficiency of Li||Cu battery and the cycle performances of the Li||LFP full batteries were tested. Owing to the excess lithium source of the coin cell, the Coulombic efficiency of the full battery hardly reflects the loss of lithium during depositing and stripping. Therefore, the Coulombic efficiency of Li||Cu battery with 3DSF was tested first. As shown in Figure 5F, the Coulombic efficiency of the Li||Cu battery with 3DSF reaches 99.0% at the current density of 1 mA/cm^2, while the Coulombic efficiency of the Li||Cu battery without 3DSF is only 93.3% after 100 cycles. It proves that after the stable 3DSF is formed, the lithium ions can be well guided for uniform deposition and the generation of dead lithium can be avoided. Long cycle electrochemical performance on the Li||LFP full battery at the current density of 3 C was carried out in Figure 5G. The battery with 3DSF has an initial capacity of 120 mAh/g and the capacity retention rate after 1,000 cycles is 92.8%, while the capacity retention rate of battery without 3DSF cycled after 1,000 cycles is only 59.4%. To match the stability of the Li metal anode at high current density, high-loading LFP (18.3 mg/cm^2) electrode was assembled for full battery testing. The rate performance with high-loading LFP was shown in Figure 5H. Compared with the battery with 3DSF, the capacity of the control sample shows a sharp decrease trend at 1 C, which proves that the lithium anode with 3DSF can still be effective at ultra-high current density. The long-term cycle performance of high-loading LFP full battery was shown in Figure 5I. The capacity of the battery with 3DSF maintains 98.2% at 1 C after 150 cycles, but the capacity of the control sample collapses to 30 mAh/g in a short period of time. The above data prove that the 3DSF

formed by the TMF can still maintain the uniform deposition of lithium ions at a high current density and suppress the generation of lithium dendrites.

In conclusion, we designed a 3DSF structure owing to the slow ion diffusion effect and the disorder homogenization effect of lithium ions under TMF with no additional costs. Lithium ions can be uniformly deposited in the form of spiral motion under the TMF, and the planarized growth of lithium metal can further induce the formation of 3DSF. This 3DSF structure can induce the bottom-up deposition of lithium ions in stable lithium channels. It can maintain good cycle performance even under the ultra-high current density of 50 mA/cm^2 for more than 1,300 cycles. This design is expected to provide new ideas for developing a new generation of high-energy density batteries.

EXPERIMENTAL PROCEDURE

Resource availability

Lead contact

Further information and requests for resources and reagents should be directed to and will be fulfilled by the lead contact, Xu Xu (xuxu@whut.edu.cn).

Materials availability

This study did not generate new unique reagents.

Data and code availability

The authors declare that data supporting the results of this study are available in the paper and supplemental information. All other data are available from the lead contact upon reasonable request.

Fabrication of 3DSF/Li

First, the commercial copper foil was washed by acetone, ethanol and deionized water, and dried in vacuum. The Cu electrode diameter was fixed at 10 mm and waiting for lithium metal deposition. The TMF and VMF are generated by the magnets purchased in Xinhongchang magnetic industry. By adjusting the number of magnets and the distance between the magnets and the cell, the magnetic induction intensity at the battery can reach 100 mT. Each tested battery will be put far enough to eliminate the additional influence of other magnets on the battery.

Materials characterizations

SEM (Pharos-0092-F) is used to characterize the morphology and structure of materials at a voltage of 10 kV, and the elemental mappings were also collected on JEOL−7100F. TEM and HRTEM were executed with a Titan G2 60–300 with EDS image corrector. Optical images are obtained by a mobile phone. *In situ* microscope images are obtained in real time by the combination of microscope and electrochemical workstation. XPS spectra were obtained from AXIS SUPRA with working voltage of 15 kV, current of 10 mA, and step length of 0.1 eV.

Electrochemical measurements

All electrochemical characterizations are based on 2,025 button cell assembled in a glovebox filled with pure argon, and operated at room temperature. A Celgard 2400 polypropylene was used as the separator. Electrolyte used to test the modified Li anode performance was 35 μL of 1.0 M LiTFSI in a liquid mixture of 1, 2-dimethoxyethane and 1, 3-dioxolane (1:1 in volume) with 1 wt% $LiNO_3$ additive. The forming 3DSF on the copper foil (deposited at a current density of 10 mA/cm^2 for 1 h under the TMF and then charged to 1 V after 10 cycles) and lithium platinum were assembled into Li||Cu battery. The Li||Li symmetric battery was assembled by depositing a certain amount of metal lithium on the

3DSF as electrodes. And the lithium metal battery without TMF treatment was set as a control sample. The diameter of both Li/Cu anodes and the control anodes is around 12 mm. Commercial LFP were used as working electrodes with 35 μL of 1.0 M LiTFSI in a liquid mixture of 1,2-dimethoxyethane, and 1,3-dioxolane (1:1 in volume) with 1 wt% $LiNO_3$ additive. The cycling measurements were performed with a multichannel battery testing system (Neware). The voltage range of Cu/Li||LFP was 2.5–4.1 V. The load of LFP cathode with low load was 2.3 mg/cm^2 and the high LFP load was 18.3 mg/cm^2. Owing to the particularity of the TMF, the magnetic field at the center of the Cu foil is actually a VMF. The difference between the two magnetic fields can be clearly seen by observing the center of the Cu foil. The deposited lithium metal at the center shows dendrite growth, and it is difficult to form a stable SEI structure after removing the metal lithium. This is also the reason that hinders this design from obtaining better performance. (Figure S13).

SUPPLEMENTAL INFORMATION

Supplemental information can be found online at https://doi.org/10.1016/j.xcrp.2022.101080.

ACKNOWLEDGMENTS

Y.L. and M.J.X. contribute equally to this work. This work was supported the National Key Research and Development Program of China (2020YFA0715000), the National Natural Science Foundation of China (52127816, 51872218), the Foshan Xianhu Laboratory of the Advanced Energy Science and Technology Guangdong Laboratory (XHT2020-003), and the Fundamental Research Funds for the Central Universities (WUT: 2020III023, 2020III050, 2021IVA123, 2021III009), the National innovation and entrepreneurship training program for college students (No. S202110497014), and Sanya Science and Education Innovation Park of Wuhan University of Technology (2020KF0021, 2020KF0024) (all the laboratories are at WUT).

AUTHOR CONTRIBUTIONS

L.Q.M, Y.Z. and X.X. conceived and supervised this project. Y.L. and M.J.X. designed the experiments, analyzed the results and wrote the manuscript. C.L.S. and L.M.C. designed and performed XPS experiments. W.Y. designed schematic diagram. C.Z. designed Comsol simulation. X.H.C. prepared the LFP cathode.All authors discussed the results and commented on the manuscript.

DECLARATION OF INTERESTS

The authors declare no competing interests.

Received: July 19, 2022
Revised: August 20, 2022
Accepted: September 12, 2022
Published: October 5, 2022

REFERENCES

1. Lin, D., Liu, Y., and Cui, Y. (2017). Reviving the lithium metal anode for high-energy batteries. Nat. Nanotechnol. *12*, 194–206.

2. Albertus, P., Babinec, S., Litzelman, S., and Newman, A. (2017). Status and challenges in enabling the lithium metal electrode for high-energy and low-cost rechargeable batteries. Nat. Energy *3*, 16–21.

3. Chen, J., Fan, X., Li, Q., Yang, H., Khoshi, M.R., Xu, Y., Hwang, S., Chen, L., Ji, X., Yang, C., et al. (2020). Electrolyte design for LiF-rich solid–electrolyte interfaces to enable high-performance microsized alloy anodes for batteries. Nat. Energy *5*, 386–397.

4. Chen, T., Kong, W., Zhao, P., Lin, H., Hu, Y., Chen, R., Yan, W., and Jin, Z. (2019). Dendrite-free and stable lithium metal anodes enabled by an antimony-based lithiophilic interphase. Chem. Mater. *31*, 7565–7573.

5. Niu, C., Pan, H., Xu, W., Xiao, J., Zhang, J.G., Luo, L., Wang, C., Mei, D., Meng, J., Wang, X., et al. (2019). Self-smoothing anode for achieving high-energy lithium metal batteries under realistic conditions. Nat. Nanotechnol. *14*, 594–601.

6. Liang, X., Pang, Q., Kochetkov, I.R., Sempere, M.S., Huang, H., Sun, X., and Nazar, L.F. (2017). A facile surface chemistry route to a stabilized lithium metal anode. Nat. Energy *2*, 17119.

7. Chen, S., Dai, F., and Cai, M. (2020). Opportunities and challenges of high-energy lithium Metal batteries for electric vehicle applications. ACS Energy Lett. *5*, 3140–3151.

8. Liu, D.H., Bai, Z., Li, M., Yu, A., Luo, D., Liu, W., Yang, L., Lu, J., Amine, K., and Chen, Z. (2020). Developing high safety Li-metal anodes for future high-energy Li-metal batteries: strategies and perspectives. Chem. Soc. Rev. *49*, 5407–5445.

9. Luo, Z., Liu, C., Tian, Y., Zhang, Y., Jiang, Y., Hu, J., Hou, H., Zou, G., and Ji, X. (2020). Dendrite-free lithium metal anode with lithiophilic interphase from hierarchical frameworks by tuned nucleation. Energy Storage Mater. *27*, 124–132.

10. Gao, Y., Yan, Z., Gray, J.L., He, X., Wang, D., Chen, T., Huang, Q., Li, Y.C., Wang, H., Kim, S.H., et al. (2019). Polymer-inorganic solid-electrolyte interphase for stable lithium metal batteries under lean electrolyte conditions. Nat. Mater. *18*, 384–389.

11. Xu, R., Cheng, X.-B., Yan, C., Zhang, X.-Q., Xiao, Y., Zhao, C.-Z., Huang, J.-Q., and Zhang, Q. (2019). Artificial interphases for highly stable lithium metal anode. Matter *1*, 317–344.

12. Cao, Z., Li, B., and Yang, S. (2019). Dendrite-free lithium anodes with ultra-deep stripping and plating properties based on vertically oriented lithium-copper-lithium arrays. Adv. Mater. *31*, e1901310.

13. Li, S.-Y., Wang, W.-P., Xin, S., Zhang, J., and Guo, Y.-G. (2020). A facile strategy to reconcile 3D anodes and ceramic electrolytes for stable solid-state Li metal batteries. Energy Storage Mater. *32*, 458–464.

14. Luo, Z., Qiu, X., Liu, C., Li, S., Wang, C., Zou, G., Hou, H., and Ji, X. (2021). Interfacial challenges towards stable Li metal anode. Nano Energy *79*, 105507.

15. Wan, M., Kang, S., Wang, L., Lee, H.W., Zheng, G.W., Cui, Y., and Sun, Y. (2020). Mechanical rolling formation of interpenetrated lithium metal/lithium tin alloy foil for ultrahigh-rate battery anode. Nat. Commun. *11*, 829.

16. Chen, L., Fan, X., Ji, X., Chen, J., Hou, S., and Wang, C. (2019). High-energy Li metal battery with lithiated host. Joule *3*, 732–744.

17. Duan, H., Zhang, J., Chen, X., Zhang, X.D., Li, J.Y., Huang, L.B., Zhang, X., Shi, J.L., Yin, Y.X., Zhang, Q., et al. (2018). Uniform nucleation of lithium in 3D current collectors via bromide intermediates for stable cycling lithium metal batteries. J. Am. Chem. Soc. *140*, 18051–18057.

18. Lee, Y.-G., Fujiki, S., Jung, C., Suzuki, N., Yashiro, N., Omoda, R., Ko, D.-S., Shiratsuchi, T., Sugimoto, T., Ryu, S., et al. (2020). High-energy long-cycling all-solid-state lithium metal batteries enabled by silver–carbon composite anodes. Nat. Energy *5*, 299–308.

19. Chi, S.S., Wang, Q., Han, B., Luo, C., Jiang, Y., Wang, J., Wang, C., Yu, Y., and Deng, Y. (2020). Lithiophilic Zn sites in porous CuZn alloy induced uniform Li nucleation and dendrite-free Li metal deposition. Nano Lett. *20*, 2724–2732.

20. Huang, G., Han, J., Zhang, F., Wang, Z., Kashani, H., Watanabe, K., and Chen, M. (2019). Lithiophilic 3D nanoporous nitrogen-doped graphene for dendrite-Free and ultrahigh-rate lithium-metal anodes. Adv. Mater. *31*, e1805334.

21. Luo, L., Li, J., Yaghoobnejad Asl, H., and Manthiram, A. (2019). A 3D lithiophilic Mo2 N-modified carbon nanofiber architecture for dendrite-free lithium-metal anodes in a full cell. Adv. Mater. *31*, e1904537.

22. Liu, S., Ji, X., Piao, N., Chen, J., Eidson, N., Xu, J., Wang, P., Chen, L., Zhang, J., Deng, T., et al. (2021). An inorganic-rich solid electrolyte interphase for advanced lithium-metal batteries in carbonate electrolytes. Angew. Chem. Int. Ed. Engl. *60*, 3661–3671.

23. Zheng, J., Engelhard, M.H., Mei, D., Jiao, S., Polzin, B.J., Zhang, J.-G., and Xu, W. (2017). Electrolyte additive enabled fast charging and stable cycling lithium metal batteries. Nat. Energy *2*, 17012.

24. Ren, X., Chen, S., Lee, H., Mei, D., Engelhard, M.H., Burton, S.D., Zhao, W., Zheng, J., Li, Q., Ding, M.S., et al. (2018). Localized high-concentration sulfone electrolytes for high-efficiency lithium-metal batteries. Chem *4*, 1877–1892.

25. Jiao, S., Ren, X., Cao, R., Engelhard, M.H., Liu, Y., Hu, D., Mei, D., Zheng, J., Zhao, W., Li, Q., et al. (2018). Stable cycling of high-voltage lithium metal batteries in ether electrolytes. Nat. Energy *3*, 739–746.

26. Wang, Q., Yao, Z., Zhao, C., Verhallen, T., Tabor, D.P., Liu, M., Ooms, F., Kang, F., Aspuru-Guzik, A., Hu, Y.S., et al. (2020). Interface chemistry of an amide electrolyte for highly reversible lithium metal batteries. Nat. Commun. *11*, 4188.

27. Liu, W., Liu, P., and Mitlin, D. (2020). Review of emerging concepts in SEI analysis and artificial SEI membranes for lithium, sodium, and potassium metal battery anodes. Adv. Energy Mater. *10*, 2002297.

28. Liu, Y., Hu, R., Zhang, D., Liu, J., Liu, F., Cui, J., Lin, Z., Wu, J., and Zhu, M. (2021). Constructing Li-rich artificial SEI layer in alloy-polymer composite electrolyte to achieve high ionic conductivity for all-solid-state lithium metal batteries. Adv. Mater. *33*, e2004711.

29. Li, N.W., Yin, Y.X., Yang, C.P., and Guo, Y.G. (2016). An artificial solid electrolyte interphase layer for stable lithium metal anodes. Adv. Mater. *28*, 1853–1858.

30. Zhai, P., Wang, T., Jiang, H., Wan, J., Wei, Y., Wang, L., Liu, W., Chen, Q., Yang, W., Cui, Y., and Gong, Y. (2021). 3D artificial solid-electrolyte interphase for lithium metal anodes enabled by insulator-metal-insulator layered heterostructures. Adv. Mater. *33*, e2006247.

31. Shadike, Z., Lee, H., Borodin, O., Cao, X., Fan, X., Wang, X., Lin, R., Bak, S.M., Ghose, S., Xu, K., et al. (2021). Identification of LiH and nanocrystalline LiF in the solid-electrolyte interphase of lithium metal anodes. Nat. Nanotechnol. *16*, 549–554.

32. Gong, Y.J., Pyo, S., Kim, H., Cho, J., Yun, H., Kim, H., Ryu, S., Yoo, J., and Kim, Y.S. (2021). Advanced Li metal anode by fluorinated metathesis on conjugated carbon networks. Energy Environ. Sci. *14*, 940–954.

33. Lang, J., Long, Y., Qu, J., Luo, X., Wei, H., Huang, K., Zhang, H., Qi, L., Zhang, Q., Li, Z., and Wu, H. (2019). One-pot solution coating of high quality LiF layer to stabilize Li metal anode. Energy Storage Mater. *16*, 85–90.

34. Kim, M.S., Zhang, Z., Rudnicki, P.E., Yu, Z., Wang, J., Wang, H., Oyakhire, S.T., Chen, Y., Kim, S.C., Zhang, W., et al. (2022). Suspension electrolyte with modified Li^+ solvation environment for lithium metal batteries. Nat. Mater. *21*, 445–454.

35. Cao, Y., Wu, Q., Wang, W., Xia, Z., Chen, Y., Zhang, B., Zou, J., and Zhu, T. (2021). A novel magnetic coupling to construct spiral deposition of lithium ions for improving anode performance of lithium-sulfur batteries. J. Electrochem. Soc. *168*, 030522.

36. Cao, Y., Wu, Q., Chen, Y., Chen, D., Liu, C., Hao, X., Zhu, T., Zhang, B., Zou, J., and Wang, W. (2021). Magnetic control of electrolyte trapping polysulfide for enhanced lithium-sulfur batteries. J. Electrochem. Soc. *168*, 070510.

37. Ren, L., Wang, A., Zhang, X., Li, G., Liu, X., and Luo, J. (2019). Eliminating dendrites through dynamically engineering the forces applied during Li deposition for stable lithium metal anodes. Adv. Energy Mater. *10*, 1902932.

38. Wang, A., Deng, Q., Deng, L., Guan, X., and Luo, J. (2019). Eliminating tip dendrite growth by lorentz force for stable lithium metal anodes. Adv. Funct. Mater. *29*, 1902630.

39. Yu, L., Wang, J., and Xu, Z.J. (2020). A perspective on the behavior of lithium anodes under a magnetic field. Small Struct. *2*, 2000043.

40. Shen, K., Wang, Z., Bi, X., Ying, Y., Zhang, D., Jin, C., Hou, G., Cao, H., Wu, L., Zheng, G., et al. (2019). Magnetic field suppressed lithium dendrite growth for stable lithium metal batteries. Adv. Energy Mater. *9*, 1900260.

41. An, S.J., Li, J., Daniel, C., Mohanty, D., Nagpure, S., and Wood, D.L. (2016). The state of understanding of the lithium-ion-battery graphite solid electrolyte interphase (SEI) and its relationship to formation cycling. Carbon *105*, 52–76.